This is the accepted manuscript made available via CHORUS. The article has been published as:

Impact of interstitial oxygen on the electronic and magnetic structure in superconducting Fe_{1+y}TeO_{x} thin films

Hefei Hu, Ji-Hwan Kwon, Mao Zheng, Can Zhang, Laura H. Greene, James N. Eckstein, and Jian-Min Zuo

Phys. Rev. B **90**, 180504 — Published 19 November 2014

DOI: 10.1103/PhysRevB.90.180504

Impact of interstitial oxygen on electronic and magnetic structure in superconducting $Fe_{1+y}TeO_x$ thin-films

Hefei Hu[1,2,4], Ji-Hwan Kwon[2,3], Mao Zheng [1,2], Can Zhang[1,2], Laura H. Greene[1,2], James N. Eckstein[1,2], Jian-Min Zuo[2,3*]

[1] Department of Physics, University of Illinois at Urbana-Champaign, Urbana, Illinois 61801, USA

[2] Frederick Seitz Materials Research Laboratory, University of Illinois at Urbana-Champaign, Urbana, Illinois 61801, USA

[3] Department of Materials Science and Engineering, University of Illinois at Urbana-Champaign, Urbana, Illinois 61801, USA

[4] Present address: Condensed Matter Physics and Materials Science Department, Brookhaven National Laboratory, Upton, New York 11973, USA

Abstract

Interstitial oxygen critical to the emergence of superconductivity in $Fe_{1+y}TeO_x$ thin-films has been detected. Its location and concentration are measured by atomic-resolution EELS with x = 0.09. The DFT calculations show that oxygen incorporation leads to local disorder in the magnetic moments of Fe, hole doping by oxygen forming ionic bonds with Fe and a large magnetic- and position-dependent increase or reduction in the Te-Fe-Te bond angles. An examination of bonding based on charge density further reveals covalent charge between Fe and Te, and its reduction with O doping.

*Corresponding author, Prof. Jian-Min Zuo (jianzuo@illiois.edu)

Superconductivity is observed in the $Fe_{1+y}TeO_x$ thin-films with T_c close to 12K after oxygen incorporation [1-6]. Oxygen substitutes Te through the introduction of oxygen during film growth [1,4,6] or occupies an interstitial site by oxygen annealing or by exposing to air after film growth [2-6]. The controlled experiment by Zheng *et al*. shows that interstitial oxygen, rather than oxygen substitution, is responsible for the emergence of superconductivity[6]. However, interstitial oxygen is difficult to detect and consequently its impact on the electronic and magnetic structure of $Fe_{1+y}TeO_x$ thin-films is largely unknown. Since oxygen doping is directly behind the emergence of superconductivity in the $Fe_{1+y}TeO_x$ thin-films, understanding the exact roles of interstitial oxygen can have a significant impact on our understanding of superconductivity in this materials system.

$Fe_{1+y}Te$ belongs to the 11 family of known Fe chalcogenide crystal structures with the high-T symmetry of P4/nmm[7]. Previous theoretical study suggested several potential interstitial sites for the interstitial oxygen[3,8,9]. However, no direct evidence of interstitial oxygen has been reported so far. The amount of oxygen in the superconducting thin-films is also unknown. X-ray absorption spectroscopy measurements indicated that the Fe valence increased from 2+ to mainly 3+ with oxygen incorporation[2,3]. This suggests a substantial amount of oxygen in the superconducting $Fe_{1+y}TeO_x$ thin-films.

Here, we report a combined experimental and theoretical study to quantify interstitial oxygen and determine its electronic structure. The $Fe_{1+y}Te$ thin-films were grown on the $LaAlO_3$ (001) substrate by molecular beam epitaxy (MBE) following details reported before [6]. The films were characterized by scanning transmission electron microscopy (STEM) combined with electron energy loss spectroscopy (EELS) and X-ray

diffraction. Density functional theory (DFT) calculations are used to model the atomic structures with oxygen incorporation, and investigate the impact of oxygen on the electronic structures for different magnetic configurations.

Superconductivity in the $Fe_{1+y}Te$ thin-films emerges with oxygen doping. However, some films remain non-superconducting even with the oxygen treatment; these films have a much higher excess Fe content due to a change in the Fe/Te flux ratio in the MBE growth. Two representative superconducting and non-superconducting films of 20 nm and 100 nm thick, respectively, were selected for study. A comparison of the typical $R(T)$ curves of superconducting and non-superconducting films is made in Fig. 1(a). The superconducting films have an onset and zero resistance transition temperatures at ~13K and 11K, respectively[6]. The reduction in resistivity as temperature decreases is broadened, which implies a softened magnetic transition[10]. In contrast, the anomaly at ~65 K in the $R(T)$ curve of the non-superconducting film is similar to that of bulk crystals, which has been attributed to a sharp magnetic and structural transition in this material[7,11,12]. The two films were characterized by X-ray diffraction. Based on the measured lattice constants and using the reported reference[13], we estimated ~4% excess Fe in the superconducting film(c ~ 6.32 Å) and ~18% excess Fe in the non-superconducting film (c ~ 6.26 Å). Thus, there is a strong correlation between the magnetic properties of $Fe_{1+y}Te$ with the amount of excess Fe [14].

Figure 1(b) shows an atomic-resolution high-angle annual dark-field (HAADF) STEM image recorded along the a-axis of the superconducting film. The film is atomically flat on the $LaAlO_3$ substrate. At the interface, additional atomic layers are sometimes observed between the FeTe film and the substrate, which most likely are

consisted of Fe. To examine whether the film is strained, we performed nano-area electron diffraction with a probe of 40 nm in diameter centered at the interface. The electron diffraction results show that the (200) reflections from the substrate and film are well separated, as seen in Fig. 1(c), indicating no obvious film strain in agreement with the X-ray reciprocal space mapping result[6]. To detect interstitial oxygen, EELS spectra were recorded along the line indicated in the inset of Fig. 2(b) at an interval distance of 0.74 Å. The experiment was performed on the JEOL2200FS at the University of Illinois, equipped with a CEOS probe corrector and an in-column Ω-energy filter[15]. Figure 2(a) shows an EELS spectrum from the $Fe_{1+y}TeO_x$ thin-film. The O-K edge together with the Te-$M_{4,5}$ and Fe-$L_{2,3}$ edges with the onset energy at ~530, 570, and 708 eV, respectively, are clearly recorded. The O-K edge integrated intensity after background subtraction using the power law model is plotted as a function of the probe position in Fig. 2(b). A clear modulation of oxygen distribution is observed from this analysis. For reference, we simultaneously recorded the HAADF intensity during the EELS acquisition, which is also plotted. The HAADF intensity peaks come from the Te atomic columns due to its large Z. Based on this, the Fe positions can be identified. The comparison between the two curves shows that oxygen signal is peaked next to the Fe atomic plane.

To estimate the amount of interstitial oxygen, the O-K edge was quantified together with Te-$M_{4,5}$ edge. The background of each signal was determined ~40 eV before the edge threshold using the power-low model. Each signal was integrated with a width of 35 eV from the edge threshold. Result shows x = 9±2% for oxygen in the superconducting thin-film. Together with the estimate of 4% excess Fe, the overall

composition was determined to be $Fe_{1+0.04}TeO_{0.09\pm0.02}$. Thus the amount of interstitial oxygen is substantially larger than the amount of excess Fe in the superconducting film.

The recorded O-K edge shows fine structures with a prepeak at ~531 eV and a main peak at ~538 eV. The O-K fine structure (see Fig. S1) is similar to the one we previously recorded in oxygen-annealed $Fe_{1.08}Te_{0.55}Se_{0.45}$, which can be interpreted as a mixture of the O-K edges in FeO and □-Fe_2O_3 [16].

To further determine the position of interstitial oxygen, as well as to study the effects of oxygen doping on the FeTe atomic and magnetic structures, DFT calculations were performed. Both WIEN2k[17] and VASP[18-20] packages were used to perform DFT calculations, and they led to consistent results. In what follows, only the VASP results are presented. The calculations were performed within the gradient approximation (GGA) and the projector augmented wave (PAW) pseudopotentials as implemented in the VASP package. The plane wave cutoff energy was 500 eV. The experimental lattice constants, a = 3.821 Å and c = 6.285 Å, were employed for the calculation[21]. A separate calculation using c = 6.32 Å, as determined by XRD, showed little changes in the results. A 2×2×1 supercell was used for modeling as shown in Fig. 3(a) and the k-point mesh was a 8×8×10 Monkhorst Pack grid. All atoms were free to move until the force tolerance of 0.02 eV/Å was reached. Oxygen was placed at the interstitial site above the center of the Fe square lattice based on our EELS evidence, at the opposite side of Te (see Fig. 3(a)), corresponding to the composition of $FeTeO_{0.125}$. The z height of oxygen was initially set to make the Fe-O bond length at 2 Å, corresponding to the bond distance expected for iron oxides. The relaxed structure is shown in Fig. 3. The oxygen after relaxation is at the top of a pyramid-like structure with 4 Fe atoms at the base. We also

considered the case that oxygen is centered within the Fe square lattice[8], but the oxygen atom at this location was unstable in agreement with previous report[3,9]. The calculation here did not include excess Fe, The impact of excess Fe is discussed separately late based on the DFT calculation results.

The ground state of FeTe is reported to be bicollinear antiferromagnetic (AFM) structure [14,22-24]. For our modeling of $FeTeO_{0.125}$, nonmagnetic, collinear AFM and bicollinear AFM structures[24] were all considered. The spin configurations of bicollinear and collinear AFM are shown in Fig 3(c) and (d), respectively. After atomic relaxation, the total energy of nonmagnetic structure is found to be about 0.15 eV/Fe higher than the other two AFM configurations. For the two AFM structures considered, the biollinear configuration is lower in energy by 20 meV/Fe.

For FeTe with the bicollinear and collinear AFM structures, Fe magnetic moment is calculated as 2.3 μ_B and 2.0 μ_B, respectively. With oxygen in the bicollinear AFM structure, we obtained for Fe ions next to oxygen, $M_{Fe1} = M_{Fe3} = 2.0\ \mu_B$, $M_{Fe5} = 1.9\ \mu_B$ and $M_{Fe6} = 2.4\ \mu_B$ (the sites are labelled as Fe1 to Fe8 in Fig. 3). The other four Fe atoms have magnetic moments varying from 2.0 μ_B to 2.2 μ_B. Notably, the magnetic disorder is accompanied with changes in the Fe-O bond length with $d_{Fe5\text{-}O} = 1.95$ Å, $d_{Fe6\text{-}O} = 2.08$ Å and $d_{Fe1\text{-}O} = d_{Fe3\text{-}O} = 1.98$ Å. In comparison, in the collinear AFM structure $M_{Fe} = 2.1\ \mu_B$ is obtained for all 4 oxygen-bonded Fe ions, and 2.0 μ_B for other 4 Fe ions inside the supercell. Furthermore, the Fe-O bond lengths are found to be the same (2.00 Å) in the collinear AFM structure. Thus, large magnetic disorder is found only in the oxygen incorporated bicollinear AFM structure.

The bond angle of Te-Fe-Te, α (see Fig. 3(b)), is also impacted by oxygen doping dependent on the magnetic structure. Previous work has shown that T_c increases as α increases with Se doping in $FeTe_{1-x}Se_x$[25]. For FeTe in the bicollinear and collinear AFM structure, α is calculated to be 96.2°/94.7° and 97.1°, respectively. Note that two bond angles in the bicollinear AFM structure are the result of structural distortion due to the lattice-magnetic interaction, which was also previously reported[26,27]. With interstitial oxygen, large changes in α are introduced. Changes in α in the bicollinear AFM case range from 0.2° to 6.2°. For a list of α values, see Table S1 in supplemental materials.

Bond distances and angles in general are determined by chemical bonding. To further examine how oxygen impacts bonding and the related electronic structure, we plot the difference charge density maps of FeTe and $FeTeO_{0.125}$ for different spin configurations in Fig. 4. The difference charge density map is calculated as $\Delta\rho = \rho_{crystal} - \rho_{atoms}$ where $\rho_{crystal}$ is the calculated charge density and ρ_{atoms} is the superimposed atomic charge density. For FeTe, the difference map shows Fe ions with negative $\Delta\rho$ with d-orbital features, whereas Te ions are polarized with positive $\Delta\rho$ away from the Fe plane. Significantly, there is an electron-accumulated region between Fe and Te, showing a strong covalent feature of the Fe-Te bonding with $\Delta\rho_{Max}$ = 0.010 e/bohr^3. In $FeTeO_{0.125}$, the oxygen show large positive $\Delta\rho$ as a negative ion, forming an ionic bond with Fe. Notably, the electron-accumulated region of the Fe-Te bond has $\Delta\rho_{Max}$ = 0.009 e/bohr^3, indicating a weakening of the Fe-Te bond by interstitial oxygen. In addition, the polarization of Te underneath the oxygen also changes, showing a

reduced polarization compared to the other Te ions. After oxygen incorporation, d-orbital feature of Fe is also slightly rotated, resulting from modification of the electronic structure in d-orbital. Since it has been suggested that the strong electronic polarizability of anion plays a crucial role in superconductivity in Fe-based superconductors[28], the bond modifications revealed here is noteworthy.

The effects of excess Fe are further studied by DFT calculations. A 2×2×1 supercell with one excess Fe was employed for modeling, corresponding to $Fe_{1+0.125}Te$. The initial excess Fe site was set according to the previous study[29]. Its height is calculated at 1.78 Å (1.65 Å, 1.66 Å for the bicollinear and collinear magnetic configurations, respectively) from the Fe layer, in agreement with previous reports[29,30]. Figure 5 shows the calculated (100) plane difference charge density maps of FeTe and FeTe with the excess Fe. The excess Fe is positively charged as evidenced by its large negative $\Delta\rho$. Positive $\Delta\rho$ is seen between the excess and host Fe atoms, in a covalent-like feature with $\Delta\rho_{Max}$ at the largest when the spins of the two Fe atoms are the same. The Fe-Te bonding weakens somewhat as measured by $\Delta\rho_{Max}$. In addition, ionic bonding between the excess Fe and the Te ions modifies the charge density of Te and its polarizability. Near the excess Fe, the Fe-Fe bond distances are also modified by a small amount, for example, $d_{\text{Fe1-Fe6}}$ decreases from 2.70 Å to 2.64 Å with the excess Fe. Full details are summarized in Table S2 and S3 in supplementary material. The excess Fe is spin-polarized [29]; there is an energy gain of ~0.4 eV/cell favoring the spin-polarized excess Fe. The magnetic moment of the excess Fe is 2.3, 2.4 and 2.3 μ_B for the nonmagnetic, collinear AFM, bicollinear AFM FeTe, respectively. Overall, the excess Fe

contributes to electron doping, a strong magnetic moment, and localized modification of bonding and related bond lengths.

In summary, we have demonstrated oxygen preferentially occupies the interstitial site, bonded to the Fe layer in a pyramid-like configuration. DFT calculations show that there are four major roles of interstitial oxygen in the emergence of superconductivity: 1) hole doping by oxygen that forms ionic bonds with Fe, 2) disruption of long-range AFM order by oxygen induced magnetic disorder in the bicollinear AFM structure, 3) increase of Te-Fe-Te bond angles in some cases and reduction in other cases and 4) weakening of Fe-Te bond. The large magnetic disorder with Fe in the bicollinear AFM state is accompanied by variations in the Fe-O bond lengths, while the interaction of oxygen with Fe in the collinear AFM state leads to smaller variations. In contrast, excess Fe contributes to electron doping, a strong magnetic moment and smaller variations in the Fe-Fe bond lengths.

Acknowledgement

This material is based upon work supported as part of the Center for Emergent Superconductivity, an Energy Frontier Research Center funded by the US Department of Energy, Office of Science, Office of Basic Energy Sciences, under award number DE-AC0298CH10886.

References

[1] W. D. Si, Q. Jie, L. J. Wu, J. Zhou, G. D. Gu, P. D. Johnson, and Q. Li, Phys. Rev. B **81**, 092506 (2010).

[2] Y. F. Nie, D. Telesca, J. I. Budnick, B. Sinkovic, and B. O. Wells, Phys. Rev. B **82**, 020508(R) (2010).

[3] Y. F. Nie, D. Telesca, J. I. Budnick, B. Sinkovic, R. Ramprasad, and B. O. Wells, J. Phys. Chem. Solids **72**, 426 (2011).

[4] Q. Li, W. D. Si, and I. K. Dimitrov, Rep. Prog. Phys. **74**, 124510 (2011).

[5] D. Telesca, Y. Nie, J. I. Budnick, B. O. Wells, and B. Sinkovic, Phys. Rev. B **85**, 214517 (2012).

[6] M. Zheng, H. Hu, C. Zhang, B. Mulcahy, J.-M. Zuo, and J. Eckstein, arXiv:1301.4696 (2013).

[7] K. -W. Yeh, T. -W. Huang, Y.-L. Huang, T. -K. Chen, F. -C. Hsu, P. M. Wu, Y. -C. Lee, Y. -Y. Chu, C. -L. Chen, J. -Y. Luo, D. -C. Yan, and M. -K. Wu Europhys Lett. **84**, 37002 (2008).

[8] K. Palandage, G. W. Fernando, Kun Fang, and A. N. Kocharian, J. Mater. Sci. **47**, 7671 (2012).

[9] Z. T. Zhang, Z. R. Yang, W. J. Lu, X. L. Chen, L. Li, Y. P. Sun, C. Y. Xi, L. S. Ling, C. J. Zhang, L. Pi, M. L. Tian, and Y. H. Zhang, Phys. Rev. B **88**, 214511 (2013).

[10] Y. Han, W. Y. Li, L. X. Cao, X. Y. Wang, B. Xu, B. R. Zhao, Y. Q. Guo, and J. L. Yang, Phys. Rev. Lett. **104**, 017003 (2010).

[11] M. H. Fang, H. M. Pham, B. Qian, T. J. Liu, E. K. Vehstedt, Y. Liu, L. Spinu, and Z. Q. Mao, Phys. Rev. B **78**, 224503 (2008).

[12] Y. Mizuguchi, F. Tomioka, S. Tsuda, T. Yamaguchi, and Y. Takano, J. Phys. Soc. Jpn. **78**, 074712 (2009).

[13] Y. Mizuguchi, K. Hamada, and O. Miura, Physics Procedia **27**, 9 (2012).

[14] W. Bao, Y. Qiu, Q. Huang, M. A. Green, P. Zajdel, M. R. Fitzsimmons, M. Zhernenkov, S. Chang, M. Fang, B. Qian, E. K. Vehstedt, J. Yang, H. M. Pham, L. Spinu, and Z. Q. Mao, Phys. Rev. Lett. **102**, 247001 (2009).

[15] J. G. Wen, J. Mabon, C. H. Lei, S. Burdin, E. Sammann, I. Petrov, A. B. Shah, V. Chobpattana, J. Zhang, K. Ran, J. -M. Zuo, S. Mishina, and T. Aoki, Microsc. Microanal. **16**, 183 (2010).

[16] H. Hu, J. -M. Zuo, M. Zheng, J. N. Eckstein, W. K. Park, L. H. Greene, J. Wen, Z. Xu, Z. Lin, Q. Li, and G. D. Gu, Phys. Rev. B **85**, 064504 (2012).

[17] P. Blaha, K. Schwarz, G. K. H. Madsen, D. Kvasnicka, and J. Luitz, *WIEN2k, An Augmented Plane Wave Plus Local Orbitals Program for Calculationg Crystal Properties* (Karlheinz Schwarz, Technische Universitat, Wien, Austria, 2002).

[18] P. E. Blöchl, Phys. Rev. B **50**, 17953 (1994).

[19] G. Kresse and J. Furthmüller, Comp. Mater. Sci. **6**, 15 (1996).

[20] J. P. Perdew, K. Burke, and M. Ernzerhof, Phys. Rev. Lett. **77**, 3865 (1996).

[21] V. P. S. Awana, A. Pal, A. Vajpayee, B. Gahtori, and H. Kishan, Physica C **471**, 77 (2011).

[22] A. Martinelli, A. Palenzona, M. Tropeano, C. Ferdeghini, M. Putti, M. R. Cimberle, T. D. Nguyen, M. Affronte, and C. Ritter, Phys. Rev. B **81**, 094115 (2010).

[23] S. L. Li, Clarina de la Cruz, Q. Huang, Y. Chen, J. W. Lynn, J. Hu, Y. -L. Huang, F. -C. Hsu, K. -W. Yeh, M. -K. Wu, and P. Dai, Phys. Rev. B **79**, 054503 (2009).

[24] F. Ma, W. Ji, J. Hu, Z. -Y. Lu, and T. Xiang, Phys. Rev. Lett. **102**, 177003 (2009).

[25] K. Horigane, H. Hiraka, and K. Ohoyama, J. Phys. Soc. Jpn. **78**, 074718 (2009).

[26] A. Martinelli, A. Palenzona, M. Tropeano, C. Ferdeghini, M. Putti, M. R. Cimberle, T. D. Nguyen, M. Affronte, and C. Ritter, Phys. Rev. B **81**, 094115 (2010).

[27] C. Fang, B. A. Bernevig, and J. Hu, Europhys Lett. **86**, 67005 (2009).

[28] G. A. Sawatzky, I. S. Elfimov, J. van den Brink, and J. Zaanen, Europhys Lett. **86**, 17006 (2009).

[29] L. Zhang, D. J. Singh, and M. H. Du, Phys. Rev. B **79**, 012506 (2009).

[30] R. Viennois, E. Giannini, D. van der Marel, and R. Černý, Journal of Solid State Chemistry **183**, 769 (2010).

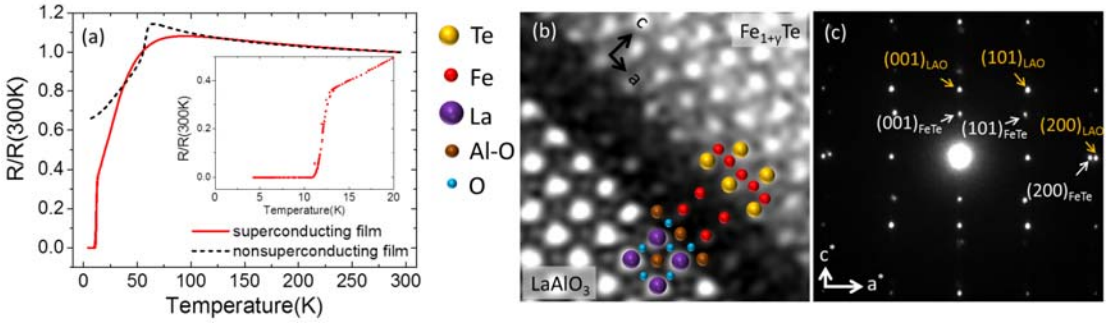

Figure 1. (a) Temperature dependence of resistivity for the superconducting and nonsuperconducting films. The inset shows an onset and zero resistance transition temperature of ~13K and 11K, respectively, for the superconducting film. (b) Atomic-resolution HAADF-STEM image of a FeTe thin-film with atomic columns labeled. (c) Electron diffraction pattern recorded from 40 nm diameter area centered at the film interface.

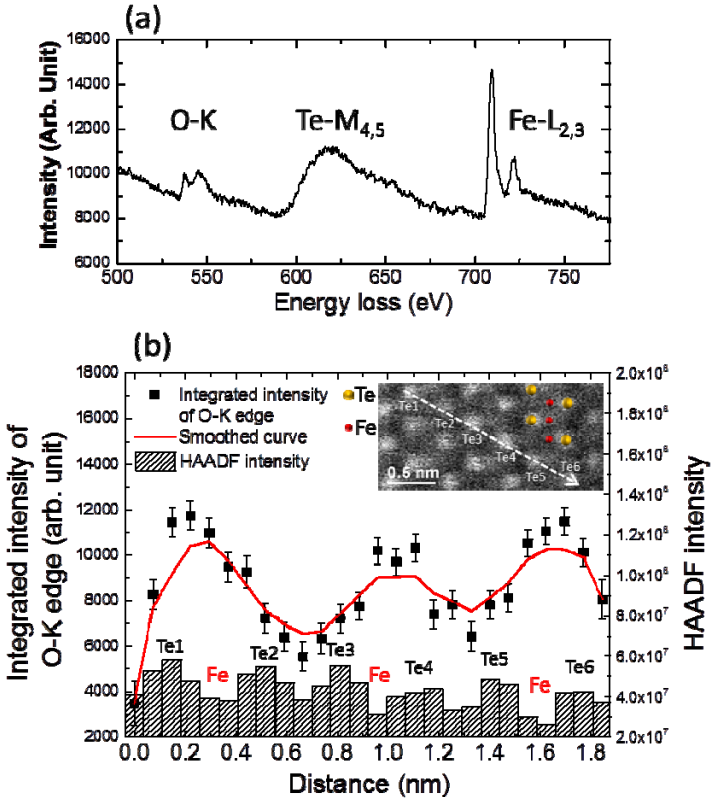

Figure 2. Line-scan EELS analysis of interstitial oxygen. (a) A typical EELS spectrum with O-K, Te-$M_{4,5}$ and Fe-$L_{2,3}$ edges labeled. (b) The integrated intensity of O-K is plotted by solid squares as a function of scan path shown on the inserted HAADF-STEM image. Error bars were estimated by assuming Poisson noise distribution for the signal and considering the standard deviation of the background intensity of the O-K. The corresponding smoothed curve is shown in red. The simultaneously recorded HAADF intensity along the scan path is shown below.

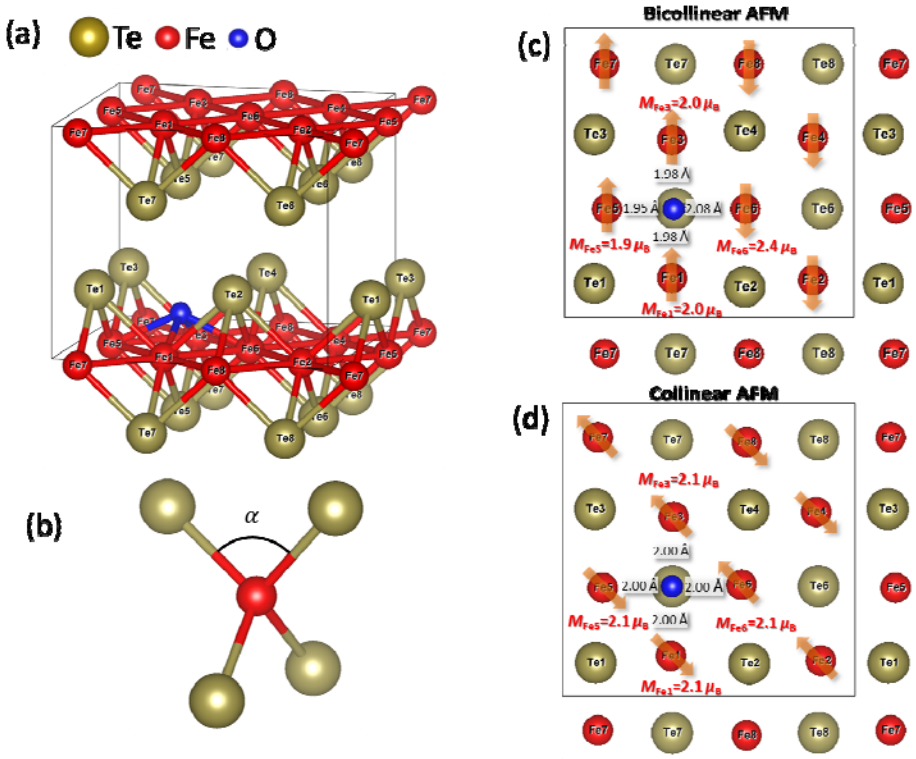

Figure 3. Structural models obtained from DFT calculations. A 2×2×1 supercell used for modeling is shown in (a) with Te-Fe-Te angle, , defined in (b). Bicollinear and collinear AFM configurations are shown in (c) and (d), respectively, with calculated Fe-O bond lengths and magnetic moments of Fe ions bonded with oxygen.

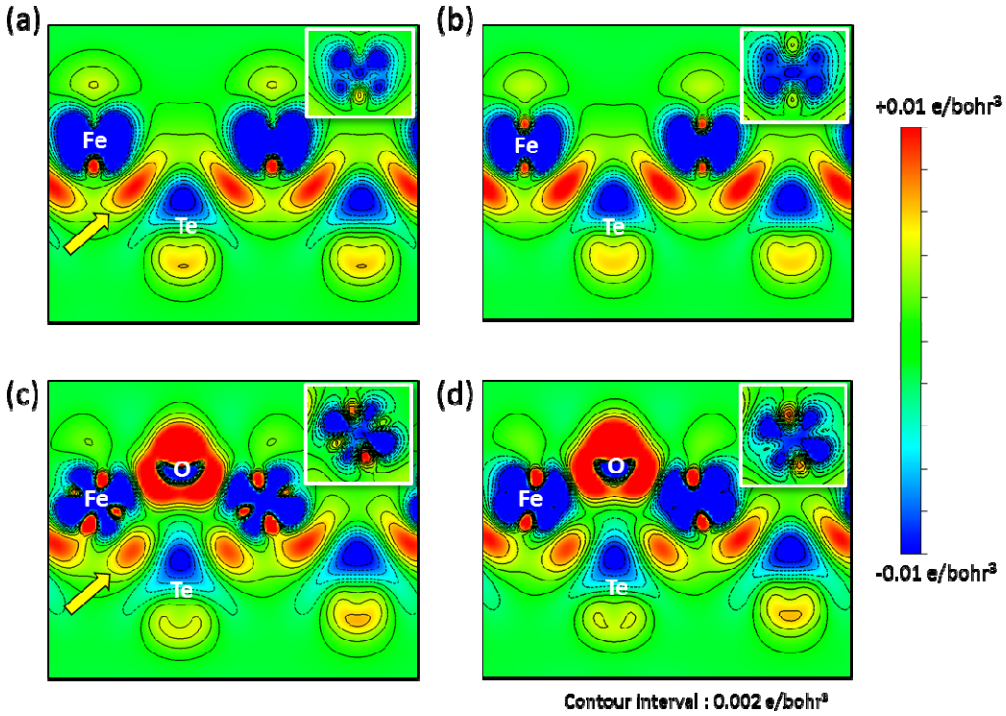

Figure 4: Difference charge density map of (a) FeTe bicollinear AFM (b) FeTe collinear AFM (c) FeTeO bicollinear AFM (d) FeTeO collinear AFM. Each inset shows difference charge density map of Fe with different scale, from -0.03 e/bohr^3 to +0.03 e/bohr^3 (contour interval: 0.005 e/bohr^3), to illustrate Fe d orbital features clearly.

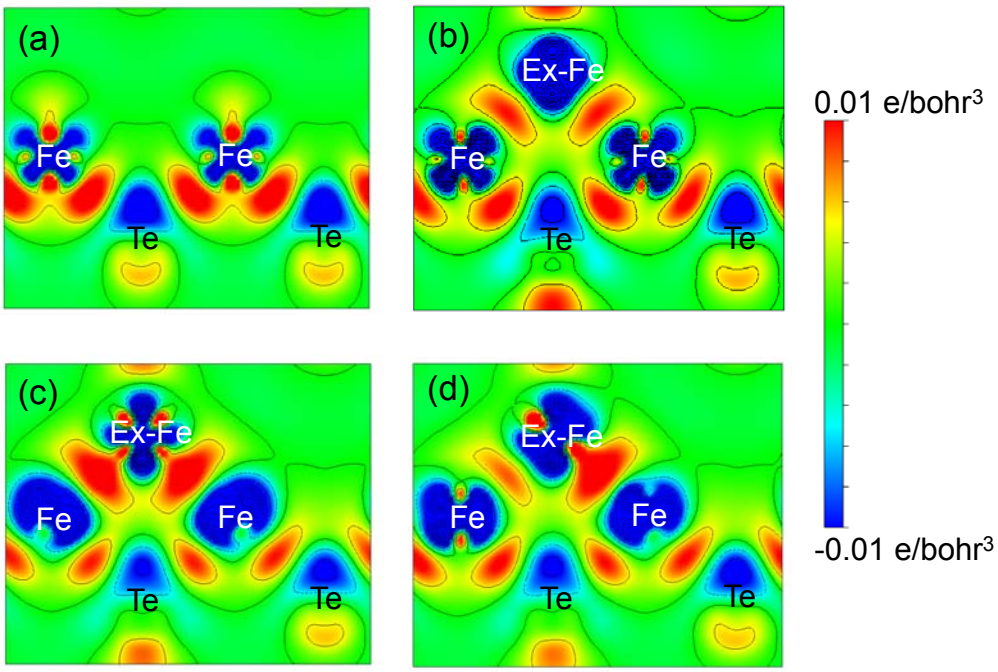

Figure 5: The effects of excess Fe on bonding as observed in the difference charge density maps of (100) plane for (a) pure FeTe, $Fe_{1.125}Te$ with (b) nonmagnetic, (c) bicollinear and (d) collinear AFM magnetic structure. Contour line is drawn from -0.08 e/bohr^3 to +0.01 e/bohr^3 at the interval of 0.005 e/bohr^3.